

Impact of Mg²⁺ and Zn²⁺ Addition on the Structural, Morphological, Physicochemical, Dielectric and Biological Properties of Hydroxyapatite

Anandhan Narayanasamy (✉ anandhan_kn@rediffmail.com)

Alagappa University <https://orcid.org/0000-0001-6783-6337>

Panneerselvam Ramaswamy

Alagappa University Faculty of Science

Poonguzhali Ramaswamy

Trinity College for Women

Amali Roselin Arockiam

Alagappa University Faculty of Science

Joseph Panneerdoss Issac

Alagappa University Faculty of Science

Ganesan Karuppannan Periannan

Alagappa University Faculty of Science

Sugumar Vasudevan

Alagappa University Faculty of Science

Research Article

Keywords: Hydroxyapatite, Dielectric, Hardness, XPS, VSM, Antibiofilm

Posted Date: October 6th, 2021

DOI: <https://doi.org/10.21203/rs.3.rs-942141/v1>

License:  This work is licensed under a Creative Commons Attribution 4.0 International License. [Read Full License](#)

Abstract

In the present work, the wet-chemical precipitation technique is employed to prepare Zinc/Magnesium doped hydroxyapatite (HA_P). In doped HA_P , the X-ray diffraction peak shifts to a higher angle because of the contraction of the lattice parameters along a -axis. The Raman peaks at 519, 440, 1464 cm^{-1} indicate the presence of Mg, Zn and CO_3^{2-} in doped HA_P respectively. The Field Emission Scanning Electron Microscopy (FESEM) measures the grain size of pure, 5% Zn and 5% Mg doped HA_P , as 275, 510, and 251 nm respectively. Transmission Electron Microscopy (TEM) confirmed the morphological change in HA_P . The X-ray photoelectron spectroscopy (XPS) identifies the presence of Mg^{2+} and Zn^{2+} in doped HA_P . The dopant elevates the hardness and dielectric constant, so the strength and the bone growth of HA_P increases. All the doped samples show excellent antibacterial, antifungal and antibiofilm activities than the pure HA_P .

1. Introduction

Hydroxyapatite [$\text{Ca}_{10}(\text{PO}_4)_6(\text{OH})_2$] (HA_P) is a biomaterial used to exchange part of a living system and giving contact to the living tissue. Bioceramic materials play a vital role in restoring and regenerating the tissues in the human body. Nano hydroxyapatite is playing important role in the hip joint, bone and dental replacements. Also, when nano biomaterial is implanted in the human body it shows outstanding osteoconductivity and osteoinduction properties. Nano HA_P delivers drugs effectively to treat bone infections [1]. Hydroxyapatite is osteoconductive but it is not osteoinductive and inherently possesses brittle nature. Further, the improvement on physiochemical and biological characteristics of HA_P is analysed by the researchers to date [2]. The presence of zinc in biological tissues induces bone mineralization and promotes pathological calcification. The Zn in the human body also plays a significant factor in the maintenance of membrane structure, function, protein synthesis, DNA synthesis, mitosis and cell proliferation [3]. Recently the cytotoxic and antibacterial activity of Zinc doped HA_P has been reported [4]. The structure of HA_P accepts the substitution of ions without any change in its hexagonal shape. But the substitution ions change the lattice parameter, crystallinity and morphology of HA_P . The nature of the substitution ions plays an important factor in the bone curing method, the addition of Zn enhances the bioactivity and antibacterial properties of pure HA_P . The Zn incorporated HA_P is more useful in orthopedics because it increases bone formation and reduces bone resorption. Substituting a high quantity of Zn with pure HA_P may cause a cytotoxic effect, so a low amount of Zn to be added with HA_P [5]. Suchanek et al. and Webster et al. found that the addition of ions changes the biophysical and chemical nature of HA_P ceramics [6 and 7]. Venkatasubbu group showed that the increase in the concentration of zinc in HA_P causes a decrease in crystallite size [8]. Wang et al. noticed the morphological change in HA_P from the hexagonal to spherical shape due to the addition of zinc [9]. Magnesium (Mg) in bone has biocompatibility with living cells and stimulates osteoblast proliferation. The lack of Mg creates bone loss. Magnesium incorporated HA_P has no cytotoxic effects [10]. Kanasan and his group observed that the increase in Mg content in HA_P elevates the microhardness [11]. Salam and his group noticed that the increase in Mg content in HA_P increases the electrical conduction and hence bioactivity of HA_P increases [12]. Even though some of the researchers have studied the Zinc and Magnesium doped HA_P they used a bulk amount of dopant. They did not heat the doped HA_P to a higher temperature, and also did not concentrate much on the studies like microhardness, magnetic behavior and antibiofilm activity. Hence, the present investigation turned to

synthesize Zn²⁺ and Mg²⁺ doped HA_P nanostructures for various concentrations by using a simple wet chemical precipitation method. The characterizations of structural, morphological, biological, mechanical, electrical, and magnetic properties of pure and incorporated HA_P are analyzed in a detailed manner.

2. Experimental Procedure

2.1. Preparation of Pure, Zn and Mg doped HA_P

In this investigation, pure and 1, 3, and 5 mole percentages of zinc and magnesium separately added nano-HA_P samples were prepared by employing the wet-chemical precipitation method. Table 1 shows the raw materials used for the preparation of pure and doped HA_P. The calcium chloride dihydrate (CaCl₂•2H₂O) and di-sodium hydrogen phosphate (Na₂HPO₄) were used as Ca²⁺ and PO₄³⁻ precursors respectively. The dopant was mixed with the CaCl₂•2H₂O solution. The pH of Ca²⁺ and PO₄³⁻ precursor solutions was maintained at 11 by using 1mole of NaOH. While Ca²⁺ precursor was maintaining at 60°C and stirring at the rate of 600 rpm, PO₄³⁻ precursor was added drop by drop into it. After washing and filtering the obtained yield was heat treated at 900°C for 2 h. All the chemicals used for the preparation of samples are from Merck India.

Table 1
Ca/P ratio and raw materials used for sample preparation.

Sample	CaCl ₂ •2H ₂ O		Na ₂ HPO ₄		Dopant		Ca/P	(Ca + dopant)/P
	gram	Mole	gram	Mole	gram	Mole		
Pure HA _P	7.351	1	4.258	0.6	NA	NA	1.67	1.67
1% ZnHA _P	7.277	0.99	4.258	0.6	0.066	0.01	1.65	1.67
3% ZnHA _P	7.130	0.97	4.258	0.6	0.198	0.03	1.61	1.67
5% ZnHA _P	6.983	0.95	4.258	0.6	0.331	0.05	1.58	1.67
1% MgHA _P	7.277	0.99	4.258	0.6	0.128	0.01	1.65	1.67
3% MgHA _P	7.130	0.97	4.258	0.6	0.385	0.03	1.61	1.67
5% MgHA _P	6.983	0.95	4.258	0.6	0.641	0.05	1.58	1.67

2.2. Characterization Techniques

X-ray diffraction (XRD) pattern was obtained for the prepared samples by employing the powder X-ray diffractometer PAN analytical X' Pert Pro, Carbatuib, WA and USA (with Cu-K α radiation, $\lambda = 1.54060 \text{ \AA}$) at 40 kV and 30 mA. FT-IR spectra were obtained with a Magna IR spectrometer 550 Nicolet over the region 4000 – 400 cm⁻¹. The morphology of the samples was analyzed by using FE-SEM analysis with EDX and it was carried out by using FEI Quanta 250 and the CZECH Republic respectively. The Micro Raman spectra of the prepared samples were obtained using a micro-Raman spectrometer and it was irradiated with a wavelength of 514.5

nm (Princeton Equipment Model: Acton SP 2500). The morphology of the samples was analysed by using TEM-Technai and G220 Twin FEI Instrument (Czech Republic). PHI VersaProbe Spectrometer was used for XPS analysis. The capacitance and the dielectric losses were estimated using the LCRZ-model TH2816A instrument. Shimadzu Model: HMV-2T was used to study the microhardness of the prepared samples. The antibacterial and antifungal activity was carried out by employing disc diffusion and well diffusion methods respectively. The antibiofilm activity was carried out against bacterial stains.

3. Results And Discussion

3.1. X-ray Diffraction (XRD) Analysis

Figures S1 and S2 show the XRD patterns of pure and ZnHA_P, pure and MgHA_P samples respectively (Refer supplementary). Figure 1 illustrates the XRD patterns of the pure, 5% Zn, and 5% Mg-doped HA_P. From the XRD pattern, the calculated lattice constants (*a* and *c*), unit cell volume (V) are in Table 2 and the crystallite size (D), microstrain (ϵ), dislocation density (ρ), the fraction of crystallinity (X_c) and specific surface area (S) are in Table 3 [13, 14]. All the XRD results are in good accord with the joint committee for powder diffraction standard (JCPDS) card # 09-432. The (0 0 2) peak position in pure HA_P slightly shifts due to the Zn or Mg dopant. Lattice parameters *a* and *b* decrease while the *c* almost remains the same due to the substitution ions, hence the (210) and (300) peak positions shift to higher angles [15]. In HA_P structure, Zn²⁺or Mg²⁺ can occupy any one of the following Ca (I), Ca (II), P and OH positions. The radius of Ca²⁺, P⁵⁻, Zn²⁺ and Mg²⁺ ions are 0.099, 0.031, 0.074, and 0.065 nm respectively. The Ca (I) and P⁵⁻ atoms form an octahedral structure with their O²⁻ atoms. But Ca (II) atoms form a tetrahedral structure with O²⁻ atoms. To form a tetrahedral structure less energy is required than to form an octahedral structure. However, the difference in ionic radius and charge of Zn²⁺and Mg²⁺ ions are more likely to replace Ca²⁺ ions. The Zn²⁺ and Mg²⁺ ions prefer Ca (II) ion to replace, due to lesser energy required in the formation of tetrahedral structure [16]. The ionic radius of Ca²⁺ is greater than Zn²⁺ and Mg²⁺. Therefore, the crystallite size decreases with an increase in dopant concentration. This result is consistent with the previous reports [8, 17, 18]. The mismatch of the ionic radius of Zn²⁺ and Mg²⁺ with the Ca²⁺creates a defect in the crystal array. Hence from the calculated values, it is found that, when the dopant concentration increased, the surface area, dislocation density and strain of the prepared samples are increasing whereas the crystallite size decreases. If the substitution ion replaced the OH ion in HA_P, the crystallite size might get increased; the decrease in crystallite size, confirms that the dopant ion replaced Ca²⁺. These results are in good accord with Miculescu et al.[19].

Table 2
Calculated lattice constants a , c and unit cell volume of the samples.

Sample	Parameter a (Å)	Parameter c (Å)	Unit cell volume (Å) 3
Pure HA _P	9.541	6.872	541.816
1%ZnHA _P	9.51	6.828	534.907
3%ZnHA _P	9.504	6.817	533.257
5%ZnHA _P	9.501	6.812	532.529
1%MgHA _P	9.616	6.85	547.544
3%MgHA _P	9.52	6.828	535.917
5%MgHA _P	9.474	6.813	529.585

Table 3
The reported values of crystallite size (D), dislocation density (ρ), strain (ε),

Sample	Crystallite Size (nm)	Dislocation Density $\times 10^{15}$ (lines/m 2)	Strain $\times 10^{-4}$ (line $^{-2} \cdot m^{-4}$)	Surface Area $\times 10^{11}$ m $^2/g$	Fraction of Crystallinity (Xc)
Pure HA _P	65.39	0.259	1.096	2.903	7.702
1%ZnH _P	62.85	0.276	1.548	3.021	6.851
3%ZnH _P	56.87	0.309	2.257	3.338	3.813
5%ZnH _P	53.83	0.345	2.603	3.527	2.418
1%MgH _P	61.4	0.265	2.113	3.092	5.435
3%MgH _P	55.86	0.321	2.703	3.399	4.299
5%MgH _P	52.35	0.382	2.854	3.626	3.677

surface area (S) and the fraction of crystallinity (Xc) for pure, Zn and Mg-doped HA_P.

3.2. FT-IR Analysis

The supplementary Figs. S3 and S4 illustrate the Fourier Transform infrared (FTIR) spectra for the prepared samples. Figure 2 illustrates the FTIR spectra of pure, 5% Zn and 5% Mg doped HA_P. Table 4 depicts the FT-IR vibrational assignment of pure, Zn and Mg doped HA_P. The presence of OH⁻ vibrations and v_1 to v_4 vibrations of PO₄³⁻ in all the FT-IR spectra confirm the hydroxyapatite structure. The FT-IR spectra of Zn/Mg doped samples are similar to the pure HA_P, but the intensity of the peak at 563 cm $^{-1}$ slightly decreases with an increase in dopant concentration. The FT-IR bands at 1590 and 1418 cm $^{-1}$ represent the carbonate in the samples. The presence of CO₃²⁻ in the samples is due to CO₂ in the air mixed with water during the preparation

of HA_P [20]. The bone structure consists of carbonate, so the presence of CO₃²⁻ increases the bioactivity of the HA_P. The intensity of the carbonate peak decreases with the increase of concentration of Zn in HA_P whereas the intensity of the carbonate peak increases with the increase of concentration of Mg in HA_P. The peaks related to the PO₄³⁻ and OH⁻ become broad while raising the concentration of both Zn²⁺ and Mg²⁺ and it indicates the decrease in crystallinity of the HA_P as obtained in XRD. Table 4 represents the PO₄³⁻, OH⁻ and CO₃²⁻ vibrational assignment. There is no vibrational indication for Zn and Mg in FT-IR spectra.

Table 4
FT-IR vibrational bands assigned to pure, Zn and Mg doped HA_P.

Pure HA _P	Zinc doped HA _P			Magnesium doped HA _P			Assignment cm ⁻¹	Reference
	1%	3%	5%	1%	3%	5%		
3574	3561	3566	3565	3571	3573	3573	OH ⁻ Stretching	15
1590	1587	1588	1588	1578	1579	1579	Carbonate ions (CO ₃ ²⁻)	20
1418	1416	1422	1422	1416	1410	1424	Carbonate ions (CO ₃ ²⁻)	2
1090	1089	1091	1086	1088	1087	1090	v ₃ Asymmetric stretching of P-O in PO ₄ ³⁻	8
1040	1042	1043	1041	1047	1047	1047	v ₃ Asymmetric stretching of P-O in PO ₄ ³⁻	15
961	955	958	959	978	965	964	v ₁ Symmetric stretching mode of P-O in PO ₄ ³⁻	17
604	602	605	605	605	605	605	v ₄ asymmetric bending mode of O-P-O in PO ₄ ³⁻	8
563	559	563	563	565	567	567	v ₄ asymmetric bending mode of O-P-O in PO ₄ ³⁻	15
472	470	471	467	461	471	471	v ₂ Symmetric bending mode of O-P-O in PO ₄ ³⁻	1

3.3. Micro Raman Analysis

Figures S5 and S6 represent the Raman spectra of pure, ZnHA_P and MgHA_P samples respectively. Figure 3 shows the Raman spectra of pure, 5% ZnHA_P and 5% MgHA_P. Table 5 depicts the Raman vibrational assignment of pure, Zn and Mg doped HA_P. Phosphate posses four vibrational modes v₁, v₂, v₃, and v₄. The vibrational modes of PO₄³⁻ present in all the Raman spectra confirm the hydroxyapatite structure in the

samples. Table 5 depicts the Raman vibrational assignment of pure, Zn and Mg doped HA_P. The FWHM of ν_1 peak (962 cm^{-1}) increases with the dopant concentration. The ν_2 peak position in doped HA_P samples shift from 459 cm^{-1} to 485 cm^{-1} and it becomes strong. The ν_3 (1035 cm^{-1}) and ν_4 (583 cm^{-1}) peaks shift to higher wavenumber. The shift of ν_2 , ν_3 , and ν_4 peak from lower to higher wavenumber is due to the following reasons; (i) the ionic radius of Ca²⁺ is more than dopant ions (ii) metal-oxygen distance of Zn and Mg, is smaller than Ca-O distance (iii) dopant ions decrease the cell volume of HA_P. The metal-oxygen distance of Ca, Zn, and Mg are 2.668, 1.875, and 1.743 Å respectively. The continuous increase in FWHM reveals an increase in crystal disorder provoked by the Zn and Mg dopants in HA_P, so the intensity of the vibrations decreases.

Furthermore, the peak at 1119 cm^{-1} and 1464 cm^{-1} indicate CO₃²⁻ present in HA_P. The ν_1 (1119 cm^{-1}) and ν_3 (1119 cm^{-1}) peaks are symmetric and asymmetric stretching vibrational modes of CO₃ respectively [22]. The insert figure f in Fig. 3 shows the ν_3 asymmetric stretching vibration of CO₃. The peaks appearing at 519 (vw) and 440 (w) cm⁻¹ are the representatives of dopants Mg and Zn respectively [23, 24]. The peaks of Zn and Mg are illustrated as insert figures d and e in Fig. 3 respectively. These results are confirmed by Popa and his groups [4]. Raman spectra results support the FT-IR results.

Table 5
Raman vibrational mode assignment of pure, Zn and Mg doped HA_P.

Pure HA _P	Zinc doped HA _P			Magnesium doped HA _P			Assignment	References
	1%	3%	5%	1%	3%	5%		
429	430	432	443	431	435	440	ν_2 doubly degenerate bending mode of PO ₄ ³⁻ (O-P-O bond)	4, 21
459	486	485	485	480	484	485	ν_4 triply degenerate bending mode of PO ₄ ³⁻ (O-P-O bond)	4
583	584	585	589	589	588	594	ν_4 triply degenerate bending mode of PO ₄ ³⁻ (O-P-O bond)	4, 21
962	964	962	965	962	966	966	ν_1 nondegenerate symmetric stretching mode of PO ₄ ³⁻ (P-O bond)	4, 21
1035	1040	1036	1036	1032	1035	1053	ν_3 triply degenerate asymmetric stretching mode of PO ₄ ³⁻ (P-O bond) and ν_1 symmetric stretching mode of CO ₃ ²⁻	4, 21, 22
1119	1123	1119	1123	1123	1129	1113	ν_1 symmetric stretching mode of CO ₃ ²⁻	22
1466	1466	1470	1468	1470	1467	1466	ν_3 asymmetric stretching mode of CO ₃ ²⁻	22

3.4. X-ray Photoelectron Spectroscopy (XPS)

XPS analysis is used to determine the oxidation state and the structural information of ZnHA_P and MgHA_P. The survey scan spectra of XPS in Fig. 4 indicates the presence of Ca, P, O, and C in all the samples and their corresponding binding energy is 347.76, 133.76, 531.37 and 285.26 eV [25, 26]. Fig. S7 shows the Ca, P, O, and C individual XPS spectra. In this spectra P, C and O have a sharp single peak, but due to spin-orbit splitting Ca has Ca2p_{3/2} and Ca2p_{1/2} two sharp peaks. The peak at 531 eV stands for O present in phosphate and the peak at 285 eV is for carbon (NIST database). The C1s (285.31 eV) peak is for adsorbed carbon. In the synthesis process, a very small amount of dopant was used, so the peaks corresponding to Zn and Mg are very weak. The XPS peak for the dopants Zn and Mg are shown as inset figures b and c in Fig. 4. Table 6 represents the BE (binding energy) of the elements in the samples. Phosphorus possesses 2p_{3/2} and 2p_{1/2} states due to spin-orbit splitting in ZnHA_P. The binding energy of Zn2p_{1/2}, Zn2p_{3/2}, 3p, and 3d in ZnHA_P XPS spectra is 1045, 1022, 45.18 and 10.35 eV respectively. Among the two Zn peaks, the 2p_{3/2} peak is tapered and is more

intensive than 2p1/2 and the area of the Zn2p3/2 peak is more than that of Zn2p1/2 due to spin-orbit (j-j) coupling. Zn2p3/2 shows degeneracy in four states, whereas Zn2p1/2 shows only in two states. The Zn2p3/2 peak is associated with a satellite peak. The satellite peak of Zn2p1/2 is located at higher binding energy approximately 23 eV than the main Zn2p3/2 peak. The binding energy of Zn2p3/2 is 1022 eV. It is nearly three times greater than the binding energy of Ca²⁺. Hence, more energy is required to substitute Ca²⁺ by Zn²⁺ during the synthesis of ZnHA_P, the required energy may be obtained either through pressure or temperature, or both. The binding energy of Mg2s and Mg2p are 88.02 and 49.4 eV respectively. There is no satellite peak for Mg. Zn and Mg binding energy results are very close to the result obtained by Negrila et al. and Predoi et al. [27, 28]. There is no remarkable change observed in the binding energy of Ca, P, and O due to the dopants. The incorporation of dopant with HA_P decreases the intensity of the Ca2p3/2 peak. It implies that dopant ions decrease the Ca²⁺ ions present on the surface. The addition of dopant ions decreases crystallinity. These results support the XRD result. No other foreign element is found in the XPS spectra. The XPS result confirmed that the dopant elements occupied the Ca²⁺ position in the HA_P structure. The XPS analysis successfully detected the presence of Zn and Mg in doped HA_P, but XRD and FT-IR did not detect these elements. XPS results support the micro Raman analysis.

Table 6
The binding energy of the Ca, P, O, C, Zn, and Mg.

Element Name	1s	2s	2p	2p _{3/2}	2p _{1/2}	3s	3p	3d	References
Ca				347.76	351.2	48.9	25.09		25, 26
P				133.76					25, 26
O		531.4							25, 26
C		285.3							25, 26
Zn				1022	1045.02		45.18	10.35	27
Mg		88.02	49.4						28

3.5. FE-SEM Analysis

Figures S8 and S9 show the FE-SEM images of pure and Zn doped HA_P and Mg doped HA_P samples respectively. Figure 5 shows the FE-SEM images of pure, 5% Zn and 5% Mg doped HA_P. Pure and doped HA_P showed cylindrical and hexagonal morphology. In Zn²⁺ doped HA_P, one-dimensional growth has been promoted. The one-dimensional growth leads to the higher thermodynamic stability of the HA_P. Because of decreasing crystallite size, grain size decreases. Micropores and porosity increase with the increase in Mg concentration in HA_P. But the addition of zinc in HA_P decreases porosity. The osteoconductivity attains an adequate level when the micropores allow the flow of extracellular fluid through the inner structure of the biomedical device. The change in grain size and a slight variation in morphology are due to the dopant ion replacing Ca²⁺ in HA_P. The grain size of pure HA_P, 5% Zn doped HA_P, and 5% Mg doped HA_P are 275, 510 and 251 nm respectively. The 5% Zn added HA_P shows highly defined rod shape morphology. Figure 6 (a, b, c)

shows the EDX spectra of pure HA_P, ZnHA_P and MgHA_P samples respectively. The sharp Ca, P and O peaks in all the spectra indicate the presence of HA_P. EDX results confirm the presence of Zn, Mg in doped HA_P. The FE-SEM results are in good accord with Kanasan et al. and Iqbal et al. findings [29, 30].

3.6. TEM Analysis

Figure 7 shows the TEM images of pure, 5% Zn and 5% Mg doped HA_P separately. The TEM images show the non-uniform and hexagonal morphology of HA_P. In Mg doped samples, the spherical morphology is more dominant than the hexagonal morphology (indicated in 7f). So, the dopant changes the morphology of HA_P. The TEM image of 5% ZnHA_P shows rod shape morphology and this result matches with the FE-SEM result. The agglomeration of particles is to decreases energy due to interfacial bonding formed by dopants [15]. Therefore, particles are composed of smaller crystallites. Figure 7 (g, h, i) represents the selected area electron diffraction (SAED) pattern of pure HA_P, 5% ZnHA_P, and 5% MgHA_P respectively. The spots and the ring patterns conform to the polycrystalline nature of hydroxyapatite. The morphology observed in TEM is in resemblance with the FE-SEM morphology.

3.7. Electrical Analysis

3.7.1. Dielectric constant

The variation of electrical capacitance and the dielectric constant, due to applied ac field is analysed. The dielectric constant (ϵ') is determined using the following formula [31].

$$\epsilon' = \frac{Ct}{\epsilon_0 A} \quad 1$$

Here C, ϵ_0 , A and t represent the capacitance, permittivity of the vacuum, area and the average thickness of the disc respectively. Figs. S10 and S11 show the variation of dielectric constant with frequency and dopant concentration. The frequency dependents dielectric constant of the pure, 5% Zn, and 5% Mg doped HA_P are given in Fig. 8. The estimated dielectric constant (ϵ') values for different frequencies are given in Table 7. The dielectric constant decrease when the frequency increases, but it increases with the increase in the concentration of dopant. In the ac field, an induced electric dipole causes polarization. The change in dielectric constant is associated with four types of polarization they are electronic polarization, ionic polarization, orientation polarization and interfacial polarization. At low frequency, the storage of charges at the grain and in grain boundary causes large interfacial polarization so, the dielectric constant is high. At higher frequencies, dipoles cannot harmonize with the applied ac field so the decrease in interfacial and orientation polarization causes a reduction in the dielectric constant. At higher frequencies, the dielectric constant is only due to electronic and ionic polarization. In HA_P electrical conduction is due to the movement of a proton between O²⁻ or an OH⁻ interacting with the PO₄ group along the c-axis. And also at elevated temperatures, OH⁻ ion in HA_P is responsible for electric conduction. At room temperature, electric conduction is due to the movement of proton in adsorbed or condensed water in HA_P [31]. The incorporation of Zn/Mg into the Ca site in the HA_P structure changes the dipole moment of the OH⁻ ions. The addition of dopant in HA_P causes shrinkage in structure, crystallographic defects and mobility of charge carriers hence the dielectric constant increases. The XRD result clearly shows that, as the dopant concentration in HA_P increases, the crystallite size decreases but defects

increase. When the dielectric constant is changed the spreading of electromagnetic fields in bone fractures is also changed. The increase in dielectric constant supports bone growth and promotes fracture healing. The Zn doped HA_P possesses a more dielectric constant than the Mg doped HA_P.

Table 7
Dielectric constants of pure and metal ions doped HA_P for different frequencies

Sample/ Frequency	30kHz	40kHz	50kHz	60kHz
Pure HA _P	1.0	0.89	0.8	0.78
1% ZnHA _P	11.66	10.46	9.62	8.92
3% ZnHA _P	12.25	11.06	10.14	9.52
5% ZnHA _P	13.23	11.95	11.03	10.26
1% MgHA _P	8.31	7.54	7.19	6.46
3% MgHA _P	9.42	8.48	7.86	7.30
5% MgHA _P	10.76	9.71	8.97	8.36

3.7.2. Dielectric loss

The dielectric material absorbs energy from the ac field, based on its capacity it holds one part of the energy and the remaining energy is lost in the form of heat at a particular frequency. This dissipated energy is considered as dielectric loss. The best dielectric material possesses the least amount of dielectric loss [32]. Figs. S12 and S13 represent the variations in dielectric loss with frequency for pure, Zn doped and Mg doped HA_P samples respectively. Figure 9 represents the variation of dielectric loss with the frequency of the sample of pure and 5% ZnHA_P, and 5% MgHA_P. The factors affecting the dielectric loss are crystal structure, applied AC frequency, temperature, stricture defects, imperfections in the crystal lattice, micro cracks, dislocations and etc. Therefore the dielectric loss can be minimized by using proper material. The dielectric loss goes on decreasing with the increase of frequency and the increase in the concentration of dopant material. At low frequency, the movement of charge carriers dominating the polarization, to rotate the dipoles more energy is required hence dielectric loss increases. In all the cases, at lower frequencies, the dielectric loss increases drastically and then decreases gradually with an increase in frequency. The deviation in dielectric loss depends on the concentration of dopants and their nature. Among Zn and Mg, at a particular frequency dielectric loss is more for ZnHA_P, less for MgHA_P. The high dielectric loss at low frequencies is due to the oscillations of the dipole. At a higher frequency, the ionic polarization ceases. Hence, the energy is not spent in rotating the dipole of the ions present in HA_P. Therefore, dielectric loss lowers.

3.7.3. AC Conductivity

Figures S14 and S15 show the variation of ac conductivity due to the applied frequency and dopant concentration of the prepared samples. The frequency dependent of ac conductivity of pure, 5% Zn, and 5% Mg

doped HA_P are given in Fig. 10. Table 8 shows the ac conductivity of pure, Zn and Mg doped HA_P at different frequencies. The ac conductivity of the materials is determined by the following relation [32].

$$\sigma_{ac} = 2\pi f \epsilon' \epsilon_0 \tan\delta \quad (2)$$

Where f is the applied frequency of ac signal, tanδ, ε' and ε₀ are the dielectric loss, dielectric constant and permittivity of vacuum respectively. Alternating current conductivity increase with increasing frequency, due to proton jumping of O²⁻ or due to the interaction of OH⁻ ion bonded with PO₄ group [33]. The AC conductivity of the sample decreases with the increase in dopant material concentration. The increase in dopant concentration causes an increase in dielectric constant and a decrease in conductivity. The results of the dielectric constant give well supports for the conductivity result. The calculated ac conductivity values are in order of 10⁻⁶ Sm⁻¹.

Table 8
Ac conductivity of the samples at different frequencies is given
in 10⁻⁶ S/m.

S. No.	Sample	Frequency			
		30 kHz	40 kHz	50 kHz	60 kHz
1	Pure HA _P	6.32	6.68	6.99	7.29
2	1% ZnHA _P	5.26	5.53	5.63	5.76
3	3% ZnHA _P	4.45	4.59	4.73	4.82
4	5% ZnHA _P	3.81	3.95	4.05	4.14
5	1% MgHA _P	4.36	4.62	4.68	4.80
6	3% MgHA _P	3.76	3.93	4.04	4.12
7	5% MgHA _P	3.25	3.42	3.49	3.56

3.8. Micro-hardness

The Vickers hardness tester is used to find the micro-hardness. All the prepared samples are made into discs separately, each of diameter 13 mm and average thickness of 2 mm. The estimated micro-hardness values, for loads 25, 50 and 100 grams are given in Table 9. The Vickers hardness (HV) can be determined by using the following relation [34].

$$H_v = 1.8544 \frac{P}{d^2} \quad (3)$$

Where P is the applied load in kg and d is the diagonal length in μm. The hardness of all the samples is increasing with the increase in load as well as the increase in dopants concentration. The addition of dopants decreases the crystallite size and increases the surface area, the driving force for densification, leading to higher mechanical properties. As the dopants are smaller in size as compared to Ca, the replacement of Ca by

dopants would reduce the bond length and increase the bond strength with O. The increase in bond strength is the cause of the increase in hardness. So the samples become more compact and harder in structure [35]. The hardness of 5% Zn²⁺ doped HA_P and 5% Mg²⁺ doped HA_P are 1059 MPa and 1081MPa respectively for a 100 gram load. At higher loads, the plastic flow of the material is less, hence the resistance offered by the material is more. Therefore, the magnitude of microhardness increases with an increase in load. The higher hardness enhances cell attachment and proliferation.

Table 9
Micro-hardness for a different load of pure, Zn and Mg doped HA_P.

Sample	Micro-hardness (Hv)		
	Load 25 g.	Load 50 g.	Load 100 g.
Pure HA _P	20.1	38.8	71.1
1%ZnHA _P	56.6	67.6	85.3
3%ZnHA _P	59.2	70.6	95
5%ZnHA _P	67.1	78	108
1%MgHA _P	59.6	64.8	79.4
3%MgHA _P	64.2	68.6	85.7
5%MgHA _P	71.7	86.9	110.3

3.9. Vibrating Sample Magnetometer (VSM)

The magnetic behavior of the prepared samples is analyzed by using a vibrating sample magnetometer with the magnetic field of – 3 to + 3 T. Figs. S16, S17, S18 and S19 represent the as-prepared and annealed sample's magnetic behavior, in the external magnetic field. Figures 11 and 12 represents the pure, 5%Zn and 5%Mg doped HA_P as prepared and annealed samples respectively. The slope of the magnetic moment and field curve gives the susceptibility of the material. It is evident from the M-H curve all the prepared samples possess negative susceptibility. The pure, doped HA_P, of as-prepared, annealed samples are diamagnetic [36]. The susceptibility of the material changes with dopant concentration. Hence, the addition of Zn²⁺/ Mg²⁺ with pure HA_P increases the mechanical properties without any change in the magnetic property.

3.10. Antibacterial Activity

The antibacterial activity of the samples is analyzed against the Gram-positive *Staphylococcus aureus* and *Streptococcus pneumoniae* and Gram-negative *Escherichia coli* and *Shigelladysenteriae* bacteria by using the disc diffusion method. Erythromycin is used as positive control and pure HA_P is used as a negative control. The zone of inhibition for each bacteria is measured and recorded in Table 10. The antibacterial activity of the samples is increased due to an increase in the concentration of dopants. And also antibacterial activity

depends on the nature of the dopants [37]. The 5% ZnHA_P and 5% MgHA_P samples show the highest zone of inhibition against *S. aureus* and *S. dysenteriae* respectively. Antibacterial activity is related to the dielectric constant and is based on charge density. The increase in dielectric constant with an increase in the concentration of dopant causes increases in charge density hence antibacterial activity increases. The positive ion interacts with negative bacteria by giving a bacterial zone. The cation of the doped element exhibits antibacterial activity and leads the biomaterial towards medical applications [38]. Figs. S20 and S21 represent the antibacterial activity zone of inhibition of ZnHA_P and MgHA_P.

Table 10
Zone of inhibition of antibacterial activity.

Sample name	Bacteria name	Zone of inhibition (mm)					Erythromycin
		1%	3%	5%	HA _P		
ZnHA _P	<i>S. dysentery</i>	13.5	14.5	15.5	12	12.5	
	E.coli	16.5	16.5	17	15	17	
	<i>S.aureus</i>	14	16	18.5	13	14	
	<i>S.pneumonia</i>	16	15.5	18	15	14	
MgHA _P	<i>S.dysentery</i>	16	18	20	13.5	14	
	E.coli	16	17	18.5	14.5	13	
	<i>S.aureus</i>	17	18	19	14	15	
	<i>S.pneumonia</i>	16	18	18.5	15	14	

3.11. Antifungal activity

The antifungal activity of the samples is investigated against the human pathogenic fungal strains *Aspergillusniger* and *Candida albicans* by well diffusion method. Here Fluconazole is used as positive control and pure HA_P is used as a negative control. The obtained antifungal results are recorded in Table 11. Furthermore, the antifungal potential of nanoparticles depends on the size and shape of the particles. The antifungal activity of *Aspergillusniger* showed a better result than *Candida albicans* in both ZnHA_P and MgHA_P. The zone of inhibition increases with the increase in the concentration of dopants. Among Zn and Mg dopants, 5%Mg doped HA_P shows the highest zone of inhibition against *Aspergillusniger*. The actual mechanism of the antifungal activity is, ZnHA_P and MgHA_P penetrate the fungal cell and hyphae, affecting the integrity of the plasma membrane. It leads to cell damage due to blocking nutrient uptake, promotion of chromosomal aberrations, mitochondrial oxidative stress and adenosine triphosphate (ATP) production is reduced. Besides, it is interrupted by fungal intracellular communication and it reduces the lifespan of fungi. Zn and Mg-doped hydroxyapatite nanoparticles are found to damage cell membranes leading to leakage of cellular components and finally cell death [39]. Figs. S22 and S23 represent the antifungal activity zone of inhibition for ZnHA_P and MgHA_P.

Table 11
Zone of inhibition of the Zn²⁺ and Mg²⁺ doped HA_P.

Sample name	Fungus name	Zone of inhibition (mm)				
		HA _P	1%	3%	5%	Fluconazole(PC)
ZnHA _P	<i>Candida albicans</i>	12	13	16	18	11
	<i>Aspergillusniger</i>	15	16	18	19	13
MgHA _P	<i>Candida albicans</i>	12	13	13	14	11
	<i>Aspergillusniger</i>	15	17	19	21	13

3.12. Antibiofilm activity

The *Staphylococcus aureus* (Gram-Positive) and *Escherichiacoli* (Gram-Negative) bacterial strains are used to analyse the antibiofilm activity of the prepared samples. Pure HA_P is used as a control. The antibiofilm activity of ZnHA_P and MgHA_P are as shown in Figs. 13 and 14 respectively. The pure HA_P treated biofilm showed dense and strong adhesive biofilm formation on the glass substrates. The density of bacterial growth decreased with an increase in dopant concentration. Notably, ZnHA_P showed a better result than MgHA_P [39]. The antibiofilm activity can be explained by stating that the ZnHA_P samples enabled in migration of radical anions into the cell membrane and reacted with the thiol group of peptides/amino acid leading to loss of cell division, mesosoma function, intracellular cell signaling, intracellular electrolytes potential, protein and DNA synthesis.

4. Conclusion

In the present work, metal ions Zn²⁺ and Mg²⁺ are separately incorporated successfully with HA_P. The physical, morphological, electrical, magnetic, antibacterial, antifungal, and antibiofilm activities of the prepared samples are investigated. The XRD, micro Raman and XPS analysis findings revealed that dopant ions successfully replaced Ca from the HA_P structure, but not in the OH position. The dopant decreases crystallite size and increases the surface area of HA_P. Hence, the hardness of HA_P increases. Subsequently, its strength and load-bearing capacity increase. The FE-SEM and TEM distinctly display the hexagonal morphology of the prepared samples. The increase in ionic polarization due to the addition of dopant in HA_P increases the dielectric constant subsequently supports the bone growth in fracture heal applications. The increase in dielectric constant leads to an increase in charge density therefore the antibacterial activity also increases. The surface defects caused due to the addition of dopant also increases the biological activity. Among all the dopants, 5% zinc doped HA_P shows the highest antibiofilm activity. The 5% magnesium doped HA_P shows the highest antibacterial and antifungal activity. The present work improved the strength, loadbearing capacity, dielectric constant and bioactivity of hydroxyapatite. Further, several analyses will be carried out in the future to improve the loadbearing capacity and the drug delivery with nanocomposites of hydroxyapatite.

Declarations

Acknowledgement

The research work done and presented in this paper is carried out with the financial support of the RUSA-Phase 2.0 grant sanctioned vide letter NO. F.24-51/2014-U, policy (TN Multi-Gen), Department of Education, Government of India, Dated 09.10.2018.

References

1. Veerla SC, Kim DR, J Kim J, *et al.* Controlled nanoparticle synthesis of Ag/Fe co-doped hydroxyapatite system for cancer cell treatment, *Mater. Sci. Eng. C* 2019, **98**: 311-323.
2. Bhattacharjee P, Begam H, Chanda A, *et al.* Animal trial on zinc doped hydroxyapatite: A case study, *J. Asian Ceram. Soc.* 2014, **2**: 44-51.
3. Iqbal N, Abdul Kadir MR, Mahmood NH, *et al.* Characterization, antibacterial and in vitro compatibility of zinc-silver doped hydroxyapatite nanoparticles prepared through microwave synthesis, *Ceram. Int.* 2014, **40**: 4507-4513.
4. Popa CL, Deniaud A, Michaud-Soret I, *et al.* Structural and biological assessment of zinc doped hydroxyapatite nanoparticles, *J. Nanomater.* 2016, Article ID 1062878, doi.org/10.1155/2016/1062878
5. Walczyk D, Malena D, Krol M, *et al.* Physicochemical characterization of zinc-substituted calcium phosphates, *Bull. Mater. Sci.* 2016, **39**: 525- 535.
6. Suchanek W, Yashima M, Kakiana M, *et al.* Hydroxyapatite ceramics with selected sintering additives, *Biomaterials* 1997, **18**: 923-933.
7. Webster TJ, Massa-Schlueter E, Smith J, *et al.* Osteoblast response to hydroxyapatite doped with divalent and trivalent cations, *Biomaterials* 2004, **25**: 2111-2121.
8. Venkatasubbu GD, Ramasamy S, Krishnan VR, *et al.* Nanocrystalline hydroxyapatite and zinc-doped hydroxyapatite as carrier material for controlled delivery of ciprofloxacin, *Biotech.* 1 (2011) 173-186.
9. Wang D, Yan T, Zhu W, *et al.* Preparation and properties of zinc-doped hydroxyapatite whisker, *J. Applied Mechanics and Materials* 2014, **487**: 131-134.
10. Tite T, Popa AC, Balescu LM, *et al.* Cationic substitutions in hydroxyapatite: Current status of the derived biofunctional effects and their In Vitro interrogation methods, *Materials* 2018, **11**: 2081. doi:10.3390/ma11112081.
11. Kanasan N, Adzila S, Koh CT, *et al.* Effects of magnesium doping of the properties of hydroxyapatite/sodium alginate biocomposite, *Adv. Appl. Ceram.* 118 (2019) 381-386.
12. Sallam SM, SaoedHanafi ME, Mohamed FA, *et al.* The dielectric study of calcium hydroxyl apatite doped by magnesium ions, *Egypt. J. Biophys. Biomed. Eng.* 2018, **19**: DOI: 10.21608/ejbbe.2018.3208.1016.
13. Gamal GA, Arabia S, Said AH, Effect of iron additives on the microstructure of hydroxyapatite, *ETASR* 2013, **3(6)**: 532-539.
14. Sundarabharathi L, Ponnamma D, Parangsan H, *et al.* Effect of anions on the structural, morphological and dielectric properties of hydrothermally synthesized hydroxyapatite nanoparticles, *SN Applied Sciences* 2020, **2(94)**: DOI: 10.1007/s42452-019-1807-3.

15. Ofudie EA, Adeogun AI, Idowu MA, *et al.* Synthesis and characterization of Zn-doped hydroxyapatite: scaffold application, antibacterial and bioactivity studies, *Heliyon* 2019, **5**:e01716.
16. Uysal I, Sevcen F, Tezcaner A, *et al.* Co-doping of hydroxyapatite with zinc and fluoride improves mechanical and biological properties of hydroxyapatite, *Prog. Nat. Sci. Mat. Int.* 2014, **24**: 340-349.
17. Popa CL, Deniaud A, Michaud-Soret I, *et al.* Structural and biological assessment of zinc doped hydroxyapatite nanoparticles, *J Nanomater*, 2016, **1**: 1-10.
18. Hanafi MES, Sallam SM, Mohamed FA, Characterization of hydroxyapatite doped with different concentration of magnesium ions, *IJRSET*. 2016, **3**: 17-23.
19. Miculescu F, Mocanu AC, Stan GE, *et al.* Influence of the modulated two-step synthesis of biogenic hydroxyapatite on biomimetic products' surface, *Appli. Surf.Sci.* 2018, **438**: 147-157.
20. Puroniene IG, Stankeviciute Z, Ishikawa K, *et al.* Formation of calcium hydroxyapatite with high concentration of homogeneously distributed silver, *Microporous Mesoporous Mater.* 2019, DOI; 10.1016/j.micromeso.2019.109806.
21. Timchenko PE, Timchenko EV, Prisareva EV, *et al.* Spectral analysis of allogeneic hydroxyapatite powders, *J. Phys. Conf. Ser.* 2017, **784**: 012060 doi:10.1088/1742-6596/784/1/012060.
22. Buzgar N, Apapel AI, The Raman study of certain carbonates, *Analele Stiintifice ale universitatii, " AL. I. CUZA" IASI Geologie*. Tomul LV, nr 2009, <https://www.researchgate.net/publication/210110408>.
23. Emayavaramban PS, Babu G, Karvembu R, *et al.* Gold nanoparticles supported on magnesium oxidnanorods for oxidation of alcohols. *JNN*. 2016, **16**: 2517-2526.
24. Gultekin D, Akbulut H. Raman studies of ZnO products synthesized by solution based methods, *Acta Phys. Plo. A* 2016, **129**: 803-805.
25. Lowry N, Han Y, Meenan BJ, *et al.* Strontium and zinc co-substituted nanophase hydroxyapatite, *Ceram. Int.* 2017, **43 (15)**: 12070-12078.
26. Lu HB, Cambell CT, Graham DJ, *et al.* Surface characterization of hydroxyapatite and related calcium phosphates by XPS and TOF-SIMS, *Anal. Chem.* 2000, **72**: 2886-2894.
27. Negrila CC, Predoi MV, Iconaru SL, *et al.* Development of zinc doped hydroxyapatite by sol-gel method for medical applications, *Molecules* 2018, **23**: 2986 doi:10.3390/molecules23112986.
28. Predoi D, Iconaru SL, Predoi MV, *et al.* Obtaining and characterizing thin layers of magnesium doped hydroxyapatite by dip coating procedure, *Coatings* 2020, **10**: 510 doi:10.3390/coatings10060510.
29. Kanasan N, Adzila S, Koh CT, *et al.* Effects of magnesium doping on the properties of hydroxyapatite/sodium alginate biocomposite, *ADV APPL CERAM* 2019, **118(7)**: 381-386.
30. Iqbal N, Iqbal S, Iqbal T, *et al.* Zinc-doped hydroxyapatite-Zeolite/Polycaprolactone composites coating on magnesium substrate for enhancing in-vitro corrosion and antibacterial performance, *Trans. Nonferrous Met. Soc. China* 2020, **30**: 123-133.
31. Khouri AEI, Zegzouti A, Elaatmani M, *et al.* Bismuth-substituted hydroxyapatite ceramics synthesis: morphological, structural, vibrational and dielectric properties, 2019, doi.org/10.1016/j.inoche.2019.107568.
32. Nayak B, Misra PK, Exploration of the structural and dielectric characteristics of a potent hydroxyapatite coated gallium bioceramics for the forthcoming biomedical and orthopedic applications, *Mater. Chem.*

- Phys. 2020, **239**: 121967. doi.org/10.1016/j.matchemphys.2020.123130.
33. Helen S, Ruban Kumar A, Study of structural, mechanical and dielectrical properties of ions doped apatite for antibacterial activity, Mater. Chem. Phys. 2019, **237**: 121867, doi.org/10.1016/j.matchemphys.2019.121867.
34. Suthar SR, Jethva HO, Joshi MJ, Vickers micro-hardness studies of Mn⁺⁺ and Cu⁺⁺ doped calcium levotartrate tetrahydrate single crystals, IOSR-JAP 2018, **10**: 5-12.
35. Sun ZP, Ercan B, Evis Z, et al. Microstructural, mechanical, and osteocompatibility properties of Mg²⁺/F⁻ doped nanophase hydroxyapatite, J Biomed Mater Res A. 2010, **93A (2)**: 411-418.
36. Chanda A, Gupta S, Vasundhara M, et al. Study of structural, optical and magnetic properties of cobalt doped ZnOnanorods. RSC Adv. 2017, **7**: 50527-50536.
37. Gayathri B, Muthukumarasamy, Delauthapilli V, et al. Magnesium incorporated hydroxyapatite nanoparticle: Preparation, characterization, antibacterial and larvicidal activity, ARAB J CHEM 2018, **11**: 645-654.
38. Helen S, Rubankumar A, Electrical, mechanical and surface analysis on ion-doped hydroxyapatite for antibacterial activity. Appl. Phys. A 2018, **124**: 535 (1-5).
39. Groza A, Ciobanu CS, Popa CL, et al. Structural Properties and Antifungal Activity against Candida albicans Biofilm of Different Composite Layers Based on Ag/Zn Doped Hydroxyapatite-Polydimethylsiloxanes. Polymers 2016, **8(131)**: 1-22.

Figures

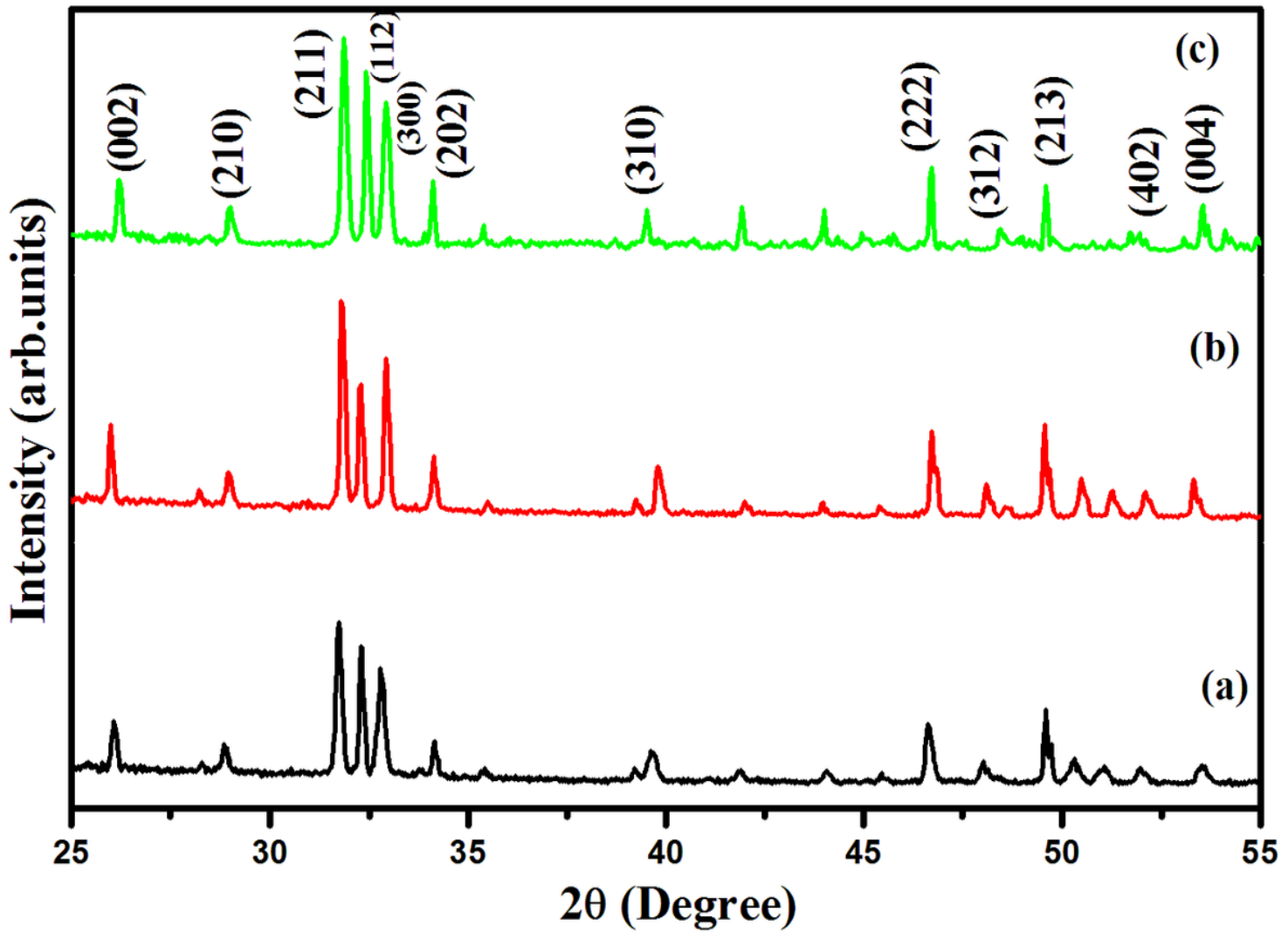


Figure 1

XRD patterns of (a) pure HAP, (b) 5% ZnHAP and (c) 5% MgHAP.

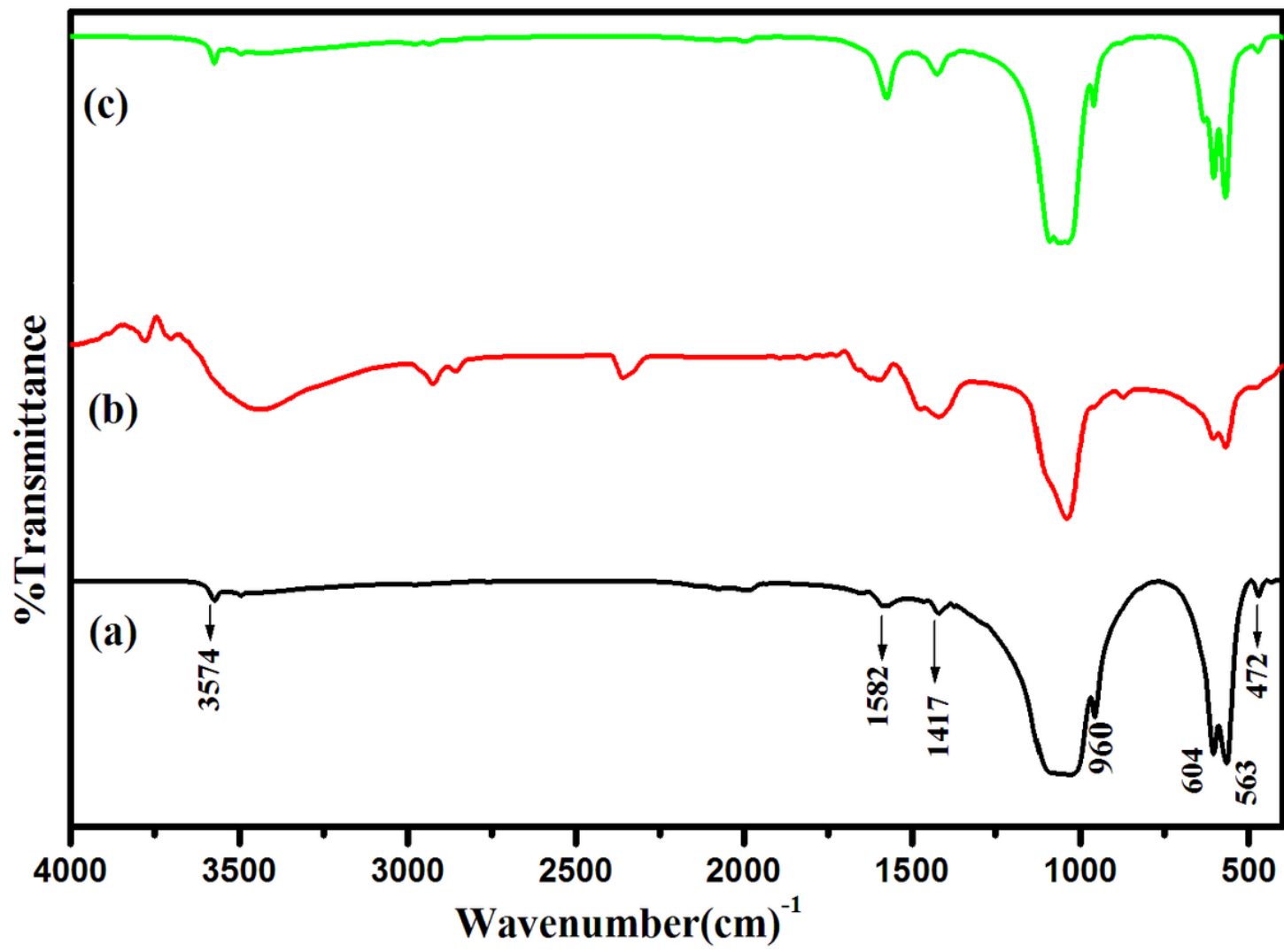


Figure 2

FT-IR spectra of (a) pure HAP, (b) 5% ZnHAP and (c) 5% MgHAP.

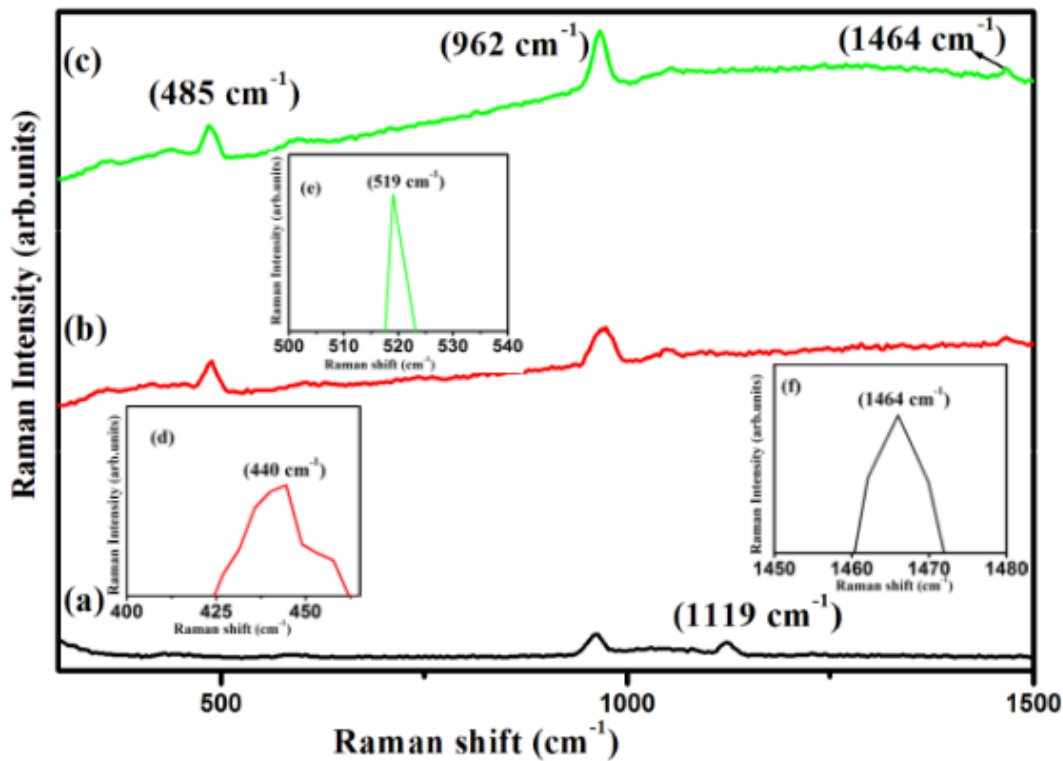


Figure 3

micro Raman spectra of (a) pure HAP, (b) 5% ZnHAP and (c) 5% MgHAP.

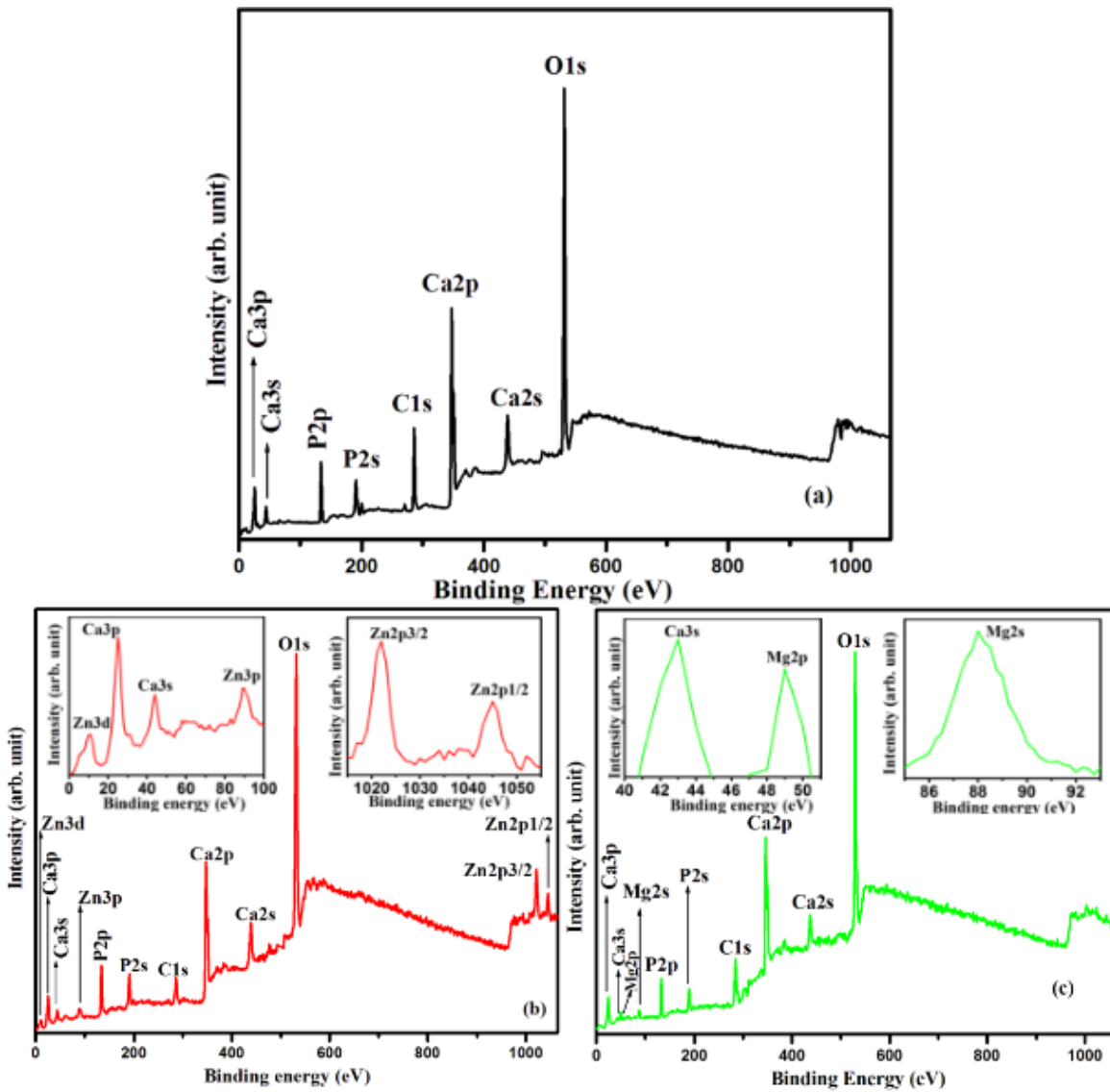


Figure 4

XPS surveys scan spectra of (a) pure HAP, (b) 5% ZnHAP and (c) 5% MgHAP

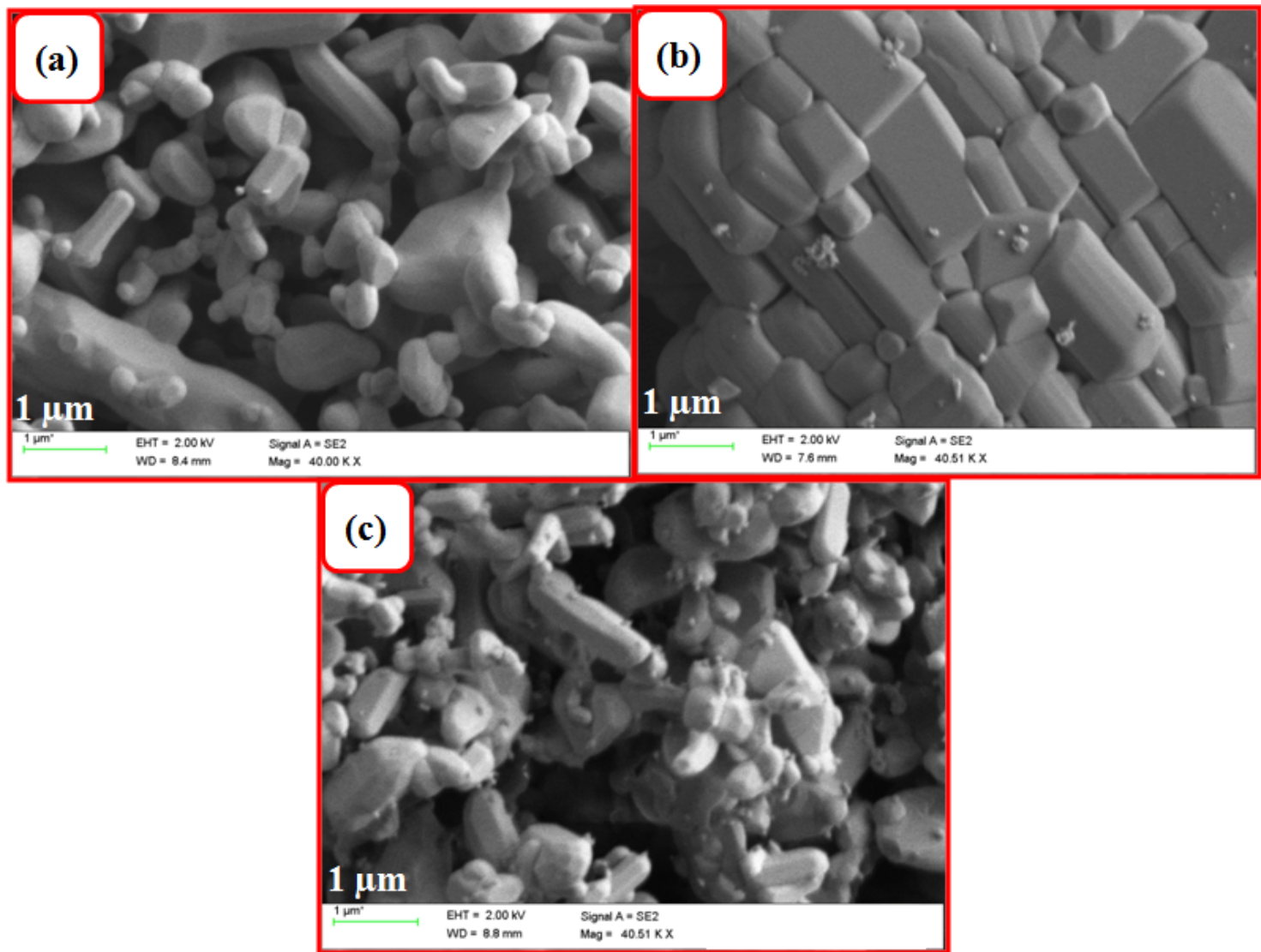


Figure 5

FE-SEM images of (a) pure HAP, (b) 5% ZnHAP and (c) 5% MgHAP.

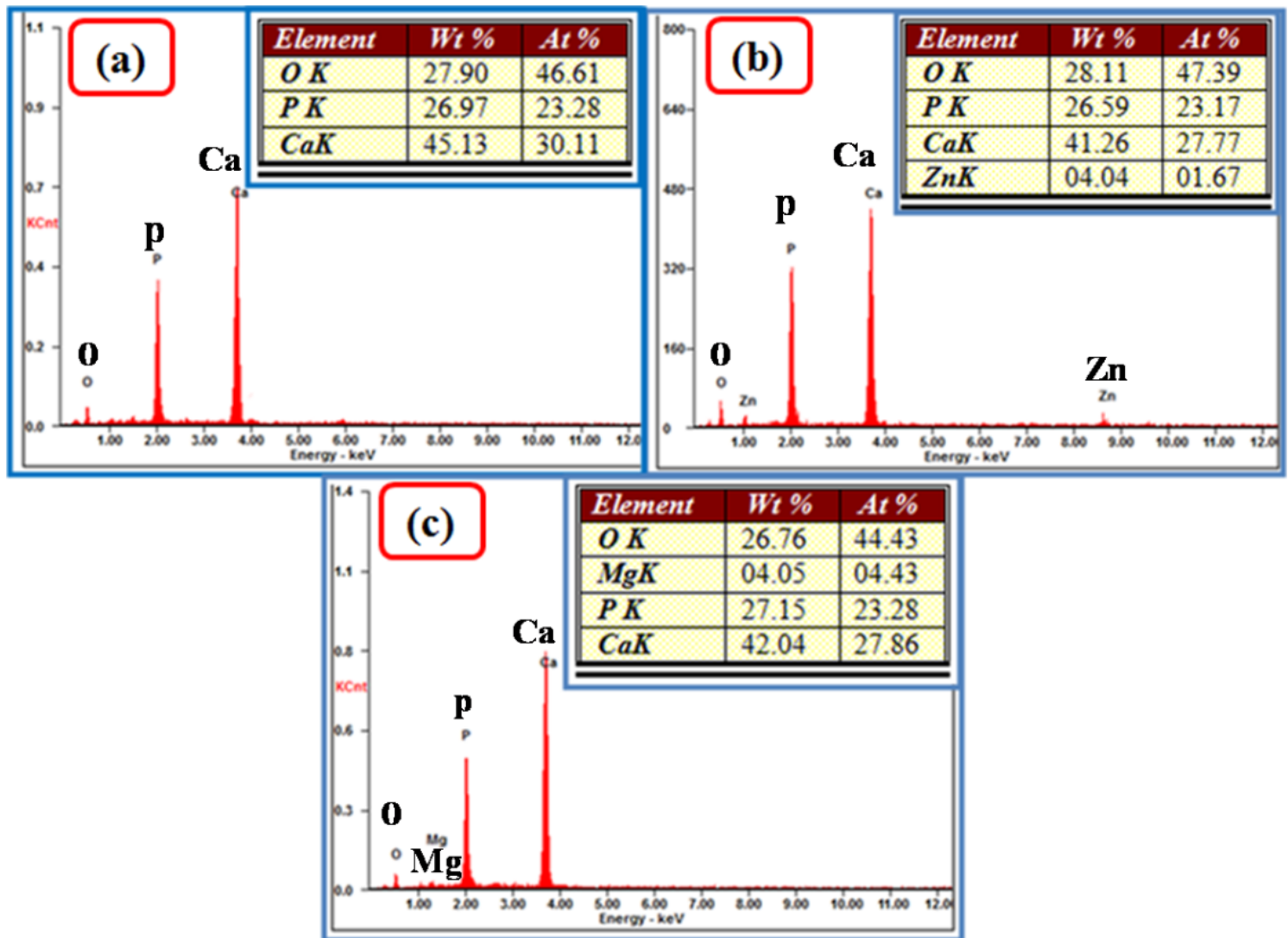


Figure 6

EDX spectra of (a) pure HAP, (b) 5% ZnHAP and (c) 5% MgHAP.

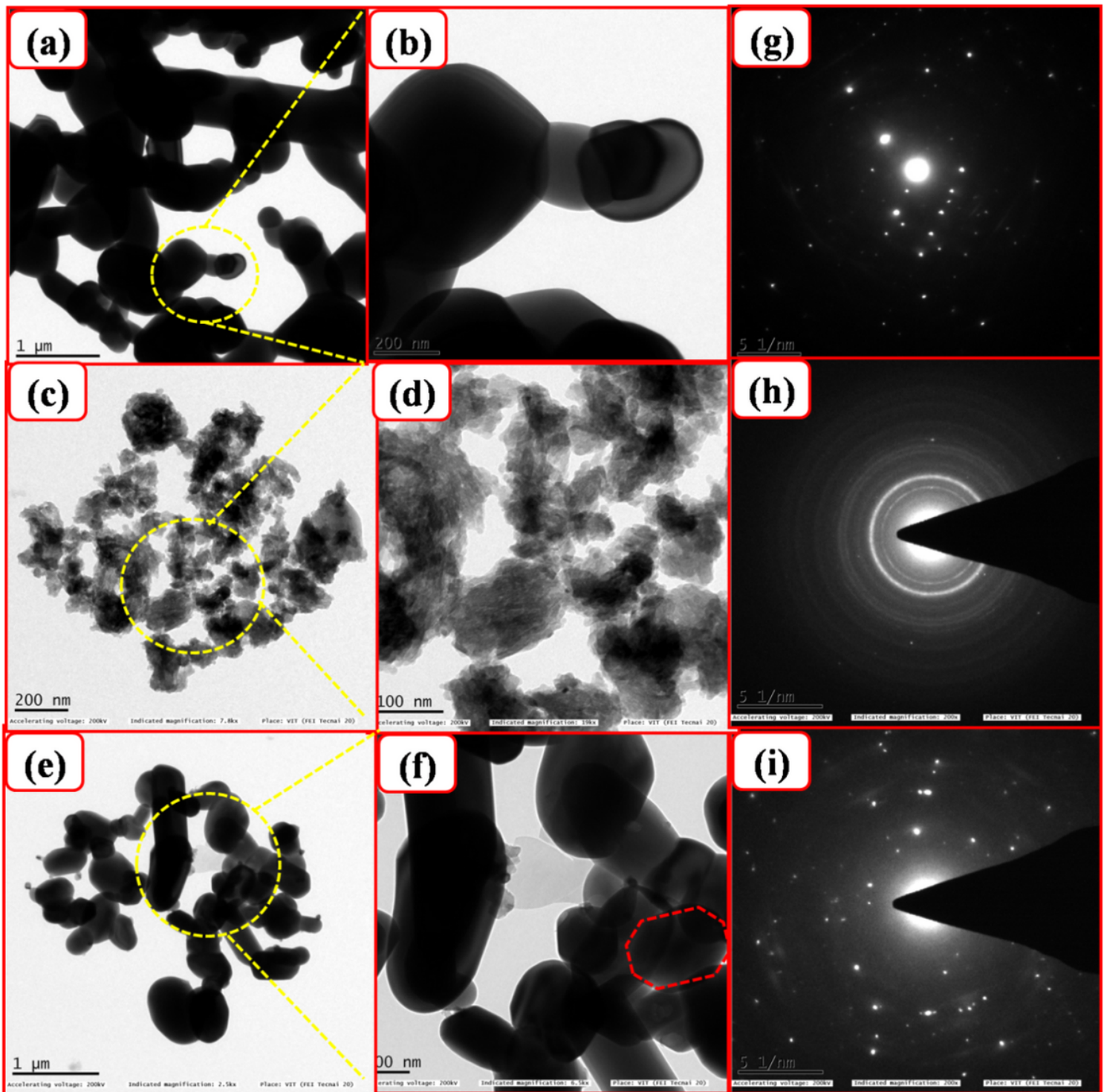


Figure 7

TEM images of (a,b) pure, (c,d) 5 % Zn and (e,f) 5% Mg doped HAP and the images g, h and i are the SEAD patterns of pure HAP, Zn and Mg doped HAP respectably.

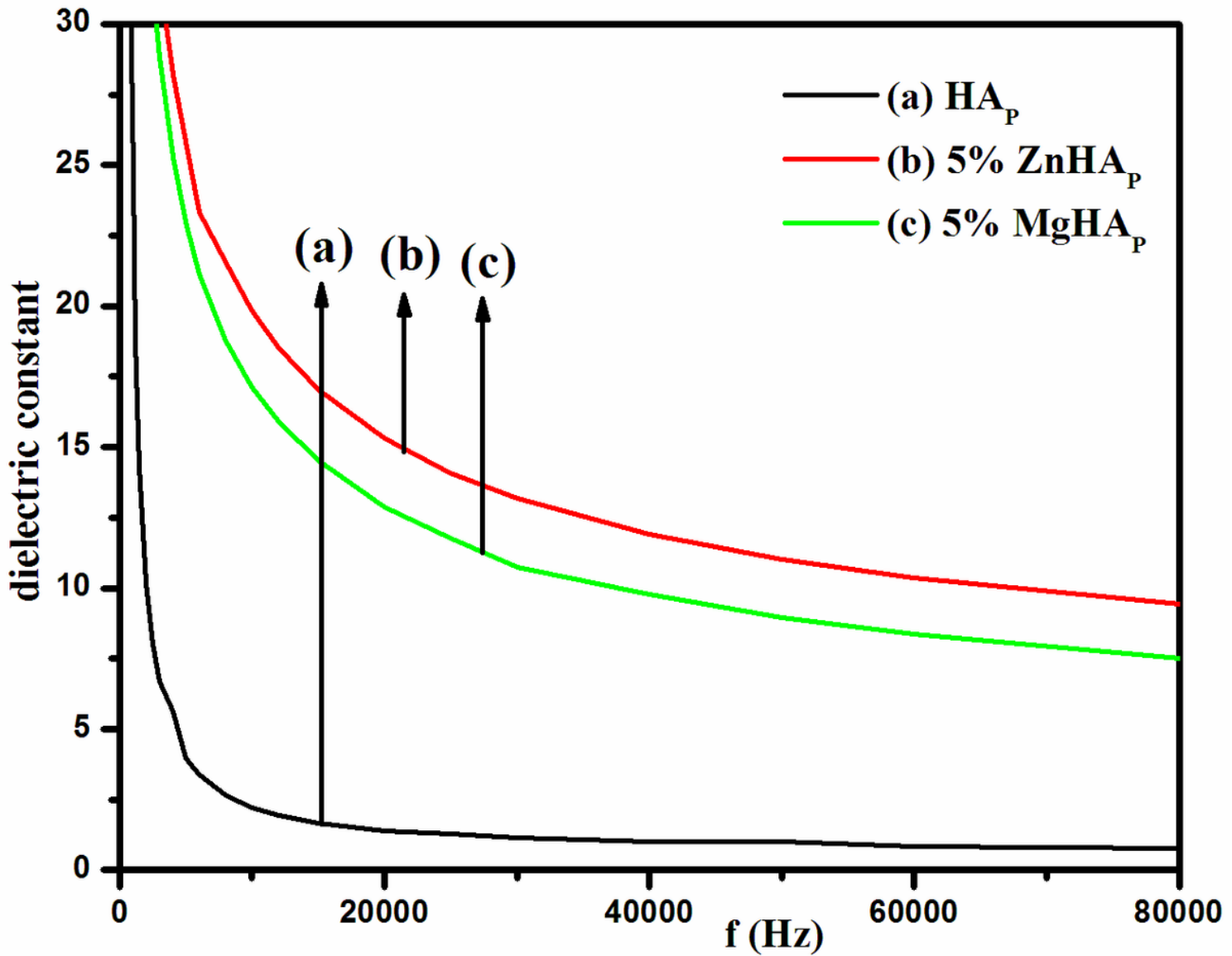


Figure 8

Dielectric Constant of pure HAP, 5% ZnHAP and 5% MgHAP with a function of frequency

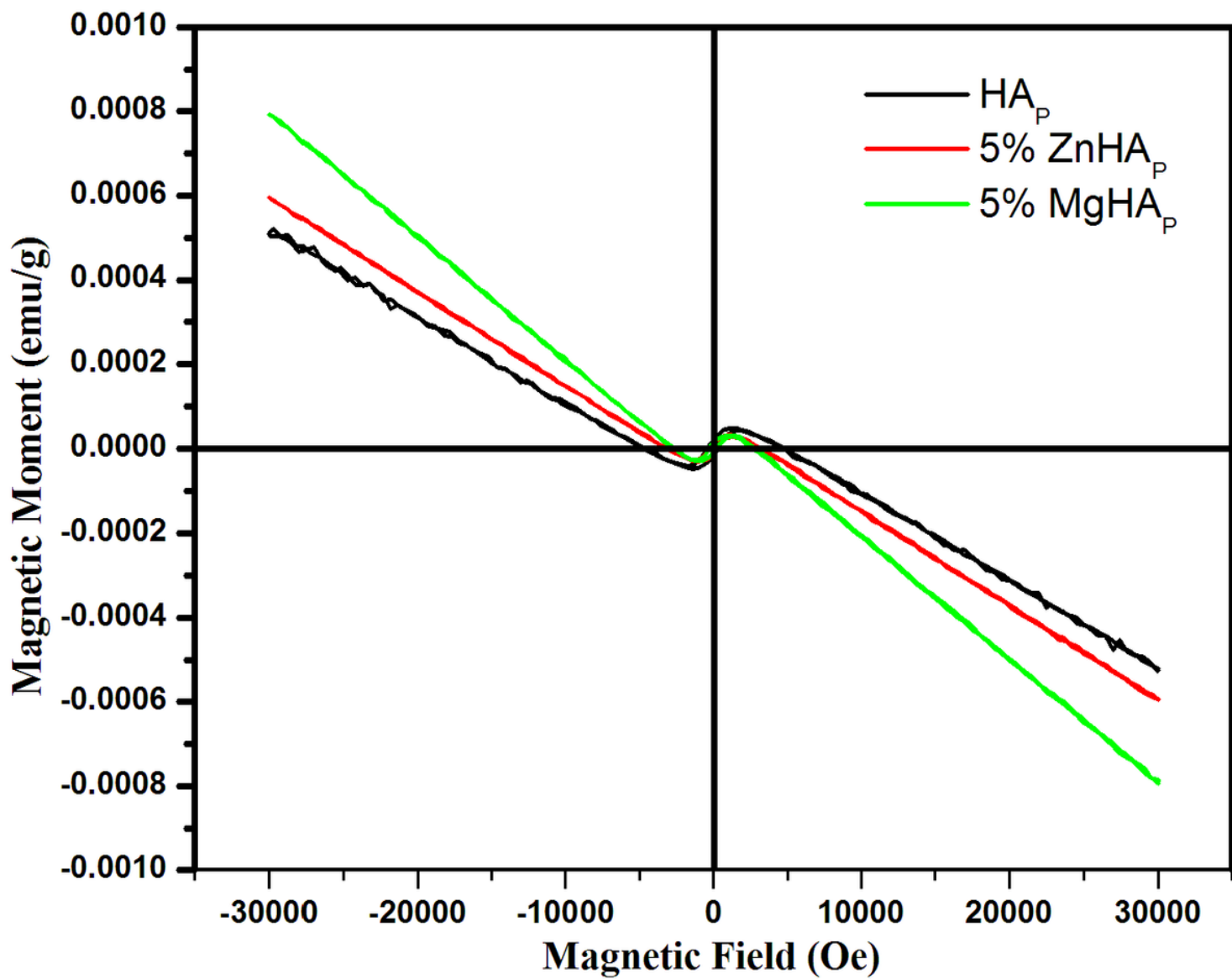


Figure 9

Dielectric loss of pure HAP, 5% ZnHAP and 5% MgHAP with a function of frequency

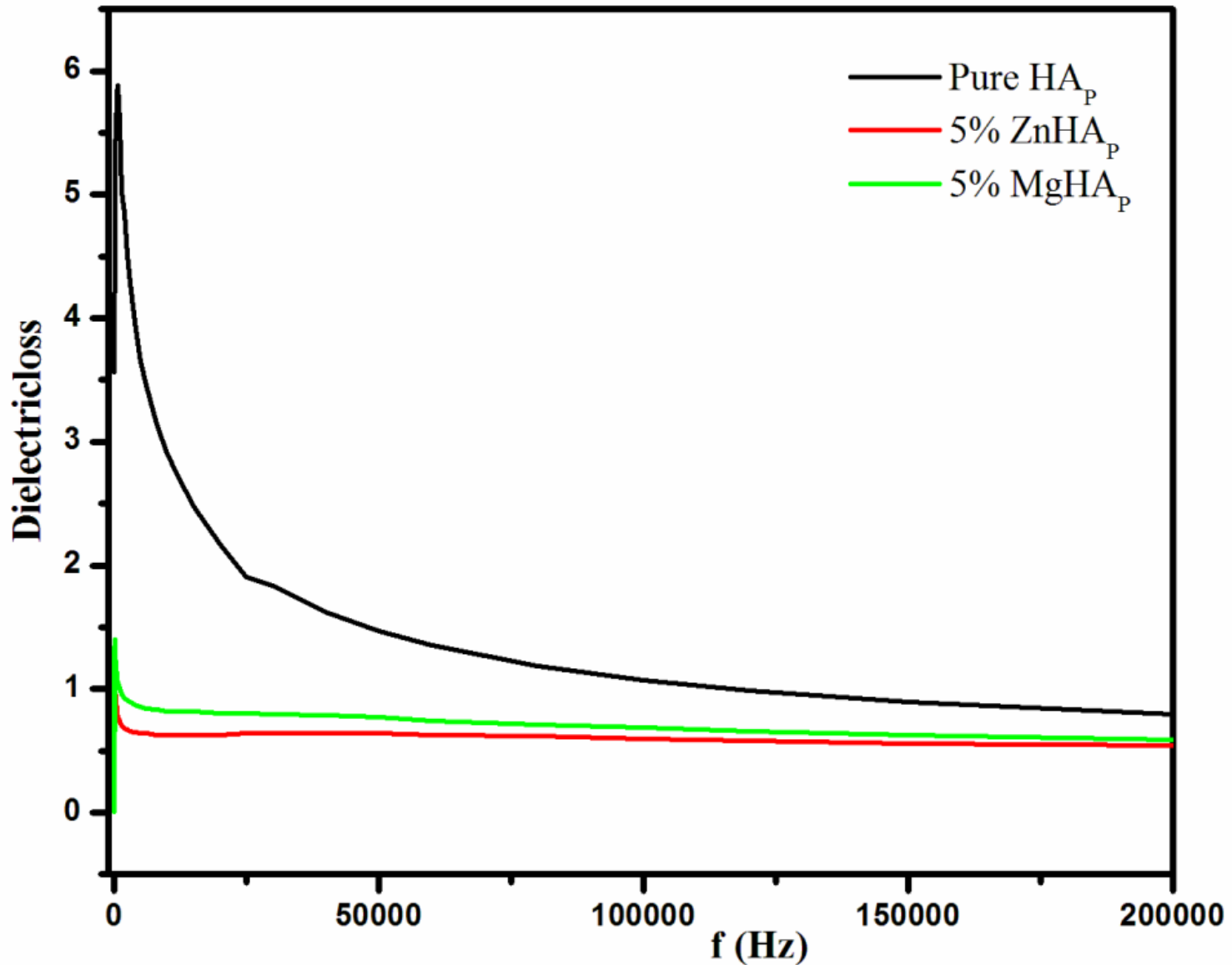


Figure 10

Conductivity as a function of the frequency of pure HAP and metal ions doped HAP.

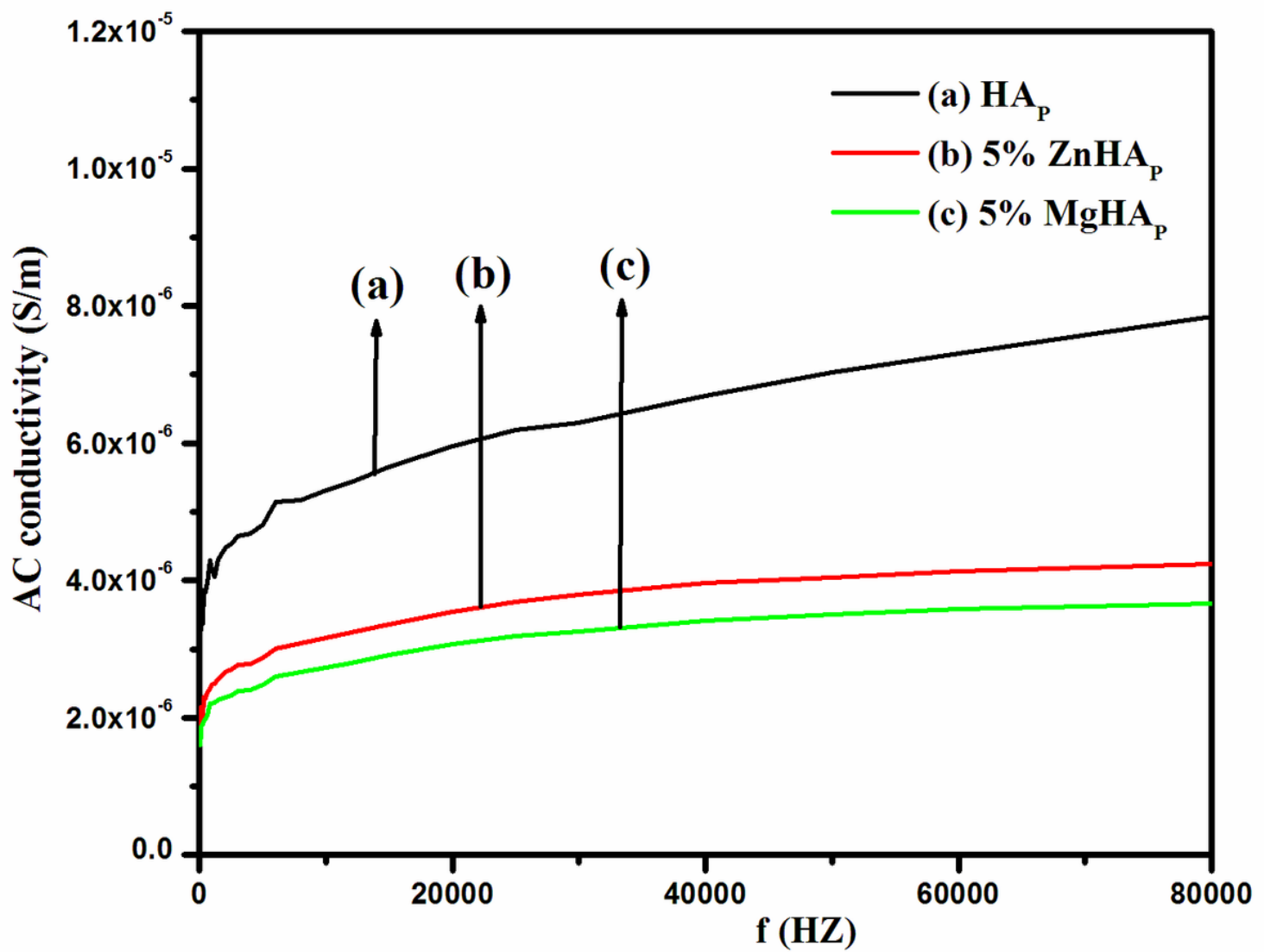


Figure 11

Magnetization Curve of the pure HAP, 5% ZnHAP, and 5% MgHAP for as-prepared samples.

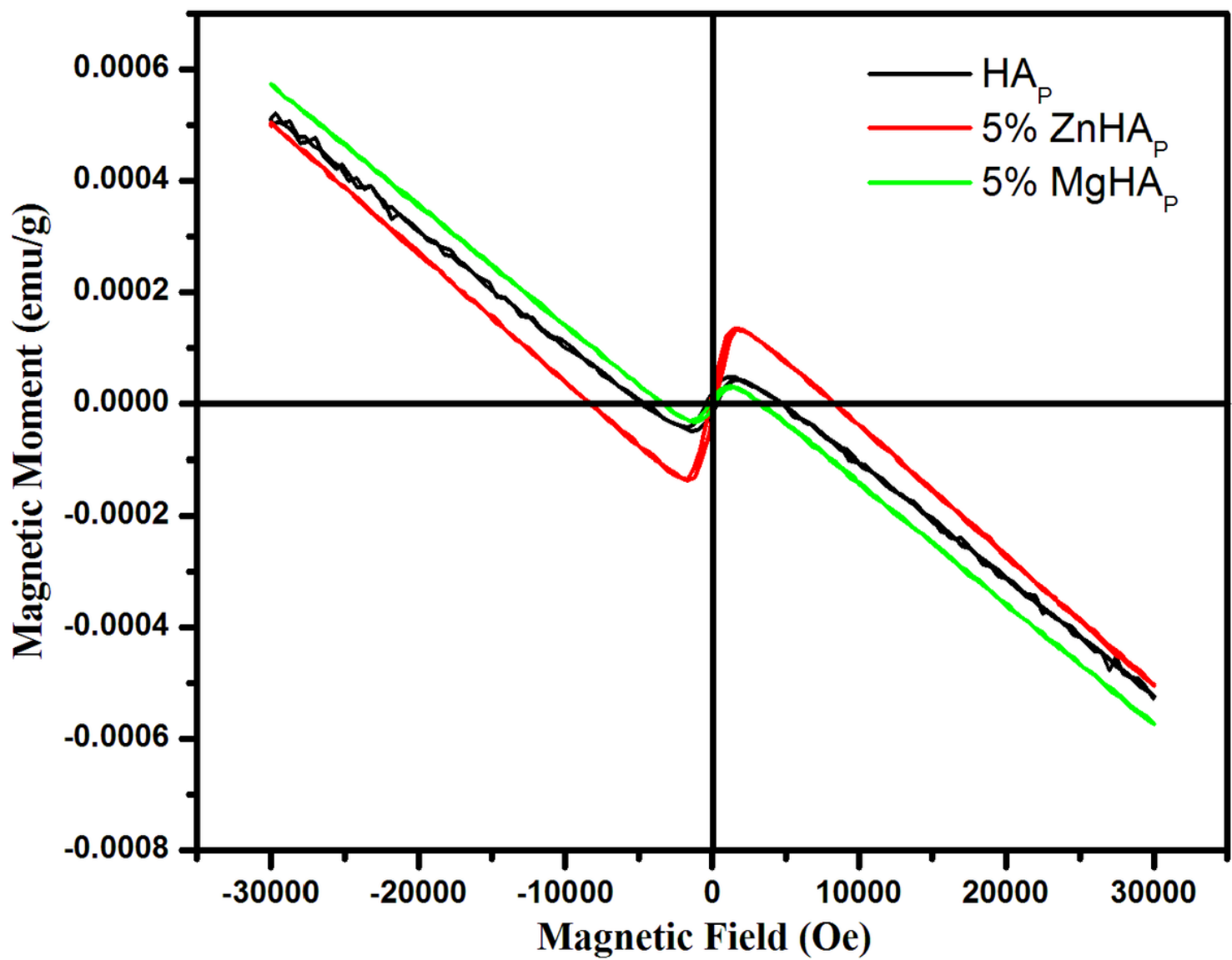


Figure 12

Magnetization Curve of pure HAP, 5% ZnHAP and 5% MgHAP annealed at 900°C.

E. coli

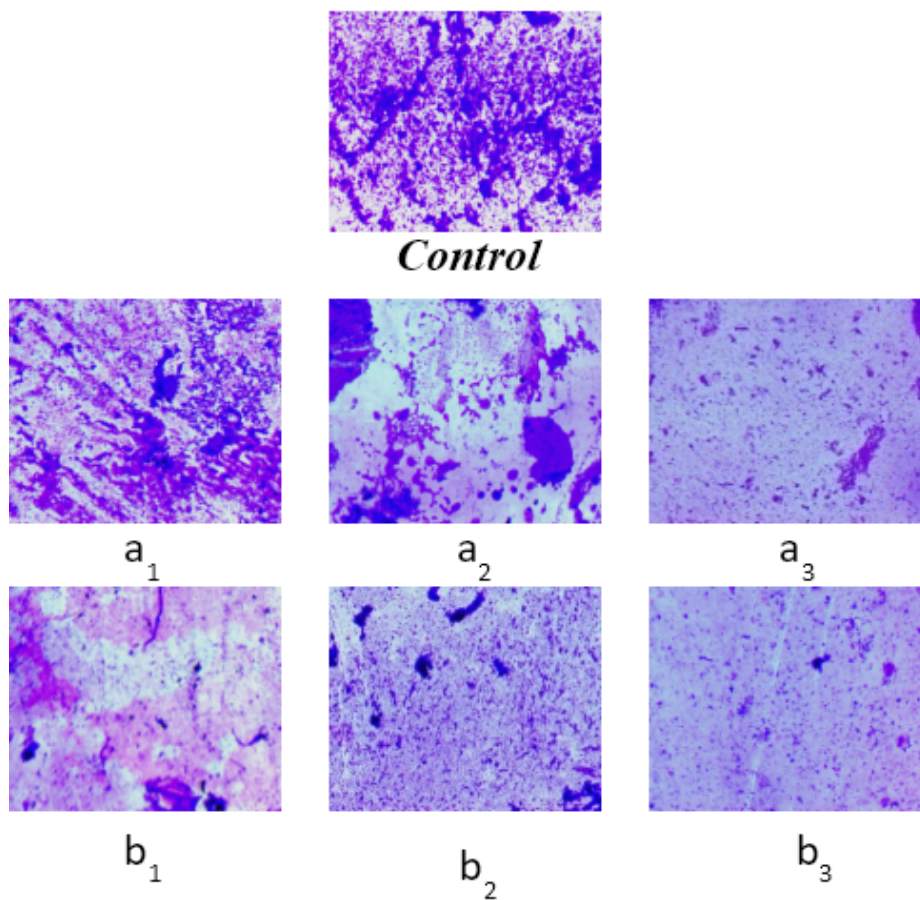


Figure 13

Antibiofilm of pure and doped HAP, a₁, a₂ and a₃ are antibiofilm of 1, 3 and 5% Zn HAP respectively. And b₁, b₂ and b₃ are antibiofilm of 1, 3 and 5% Mg HAP respectively.

S. aureus

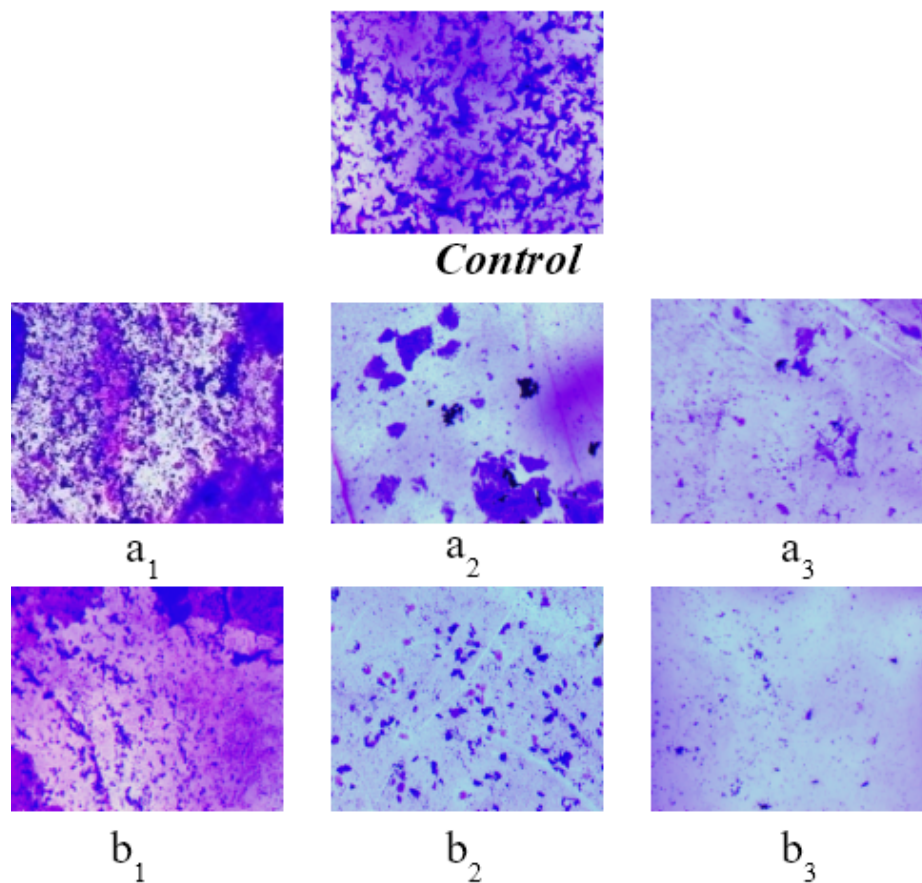


Figure 14

Antibiofilm of pure and doped HAP a1, a2 and a3 are antibiofilm of 1, 3 and 5% Zn HAP respectively. And b1, b2 and b3 are antibiofilm of 1, 3 and 5% Mg HAP respectively.

Supplementary Files

This is a list of supplementary files associated with this preprint. Click to download.

- [Supplimentery.doc](#)